ELSEVIER

Volume 180, Number 11, November 2007

JOURNAL OF SOLID STATE CHEMISTRY

www.elsevier.com/locate/jssc

CONTENTS

Abstracted/indexed in BioEngineering Abstracts, Chemical Abstracts, Coal Abstracts, Current Contents/Physics, Chemical, & Earth Sciences, Engineering Index, Research Alert, SCISEARCH, Science Abstracts, and Science Citation Index. Also covered in the abstract and citation database SCOPUS®. Full text available on ScienceDirect®.

Regular Articles

Structures and crystal chemistry of the double perovskites $Ba_2LnB'O_6$ (Ln = lanthanide $B' = Nb^{5+}$ and Ta^{5+}): Part I. Investigation of Ba_2LnTaO_6 using synchrotron X-ray and neutron powder diffraction
Paul J. Saines, Jarrah R. Spencer, Brendan J. Kennedy and Maxim Avdeev
page 2991

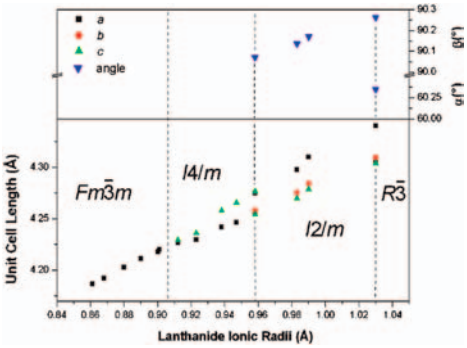

The evolution of the structure across the series of double perovskites Ba_2LnTaO_6 is established using a combination of synchrotron X-ray and neutron diffraction. The symmetry increases from monoclinic to tetragonal and then cubic as the size of the lanthanide decreases.

Structures and crystal chemistry of the double perovskites $Ba_2LnB'O_6$ (Ln = lanthanide and B' = Nb, Ta): Part II—Temperature dependence of the structures of $Ba_2LnB'O_6$
Paul J. Saines, Jarrah R. Spencer, Brendan J. Kennedy, Yoshiki Kubota, Chiharu Minakata, Hiroko Hano, Kenichi Kato and Masaki Takata
page 3001

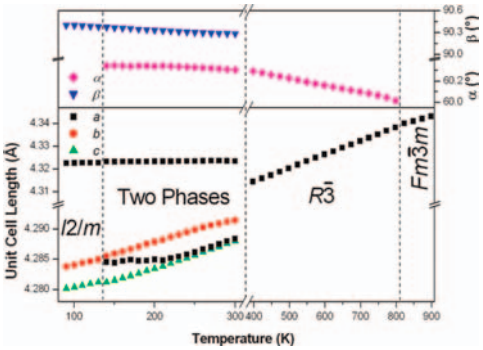

Variable temperature structural studies of Ba_2LaTaO_6 show the presence of a unexpected rhombohedral phase. Other $Ba_2LnB'O_6$ (B' = Nb, Ta) have an tetragonal intermediate phase.

Regular Articles—Continued

Designed synthesis of cobalt and its alloys by polyol process
R.J. Joseyphus, T. Matsumoto, H. Takahashi, D. Kodama, K. Tohji and B. Jeyadevan
page 3008

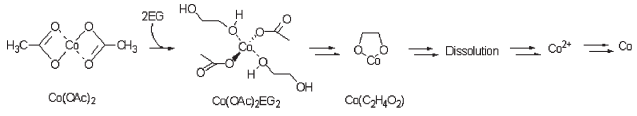

The role of polyol, precursor and reaction promoting agents in the synthesis of metal and alloy nanoparticles using polyol process has been investigated by analyzing the reaction steps involved in the synthesis of cobalt in Co ion-polyol-[OH^-] system. Figure explains the entire reaction scheme in the formation of Co metal in ethylene glycol.

The synthesis and crystal structures of the first rare-earth alkaline-earth selenite chlorides $MNd_{10}(SeO_3)_{12}Cl_8$ (M = Ca and Sr)
P.S. Berdonosov, A.V. Olenev, V.A. Dolgikh and P. Lightfoot
page 3019

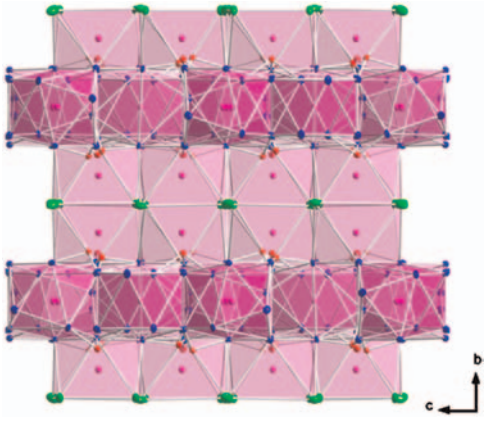

Two new alkaline-earth Nd selenite chlorides $MNd_{10}(SeO_3)_{12}Cl_8$ (M = Ca, Sr) were synthesized. These structures are constructed by $[M_{11}(SeO_3)_{12}]^{8+}$ slabs separated by chloride anion layers.

Low-temperature single crystal X-ray diffraction and high-pressure Raman studies on $[(CH_3)_2NH_2]_2[SbCl_5]$
Maciej Bujak and Ross J. Angel
page 3026

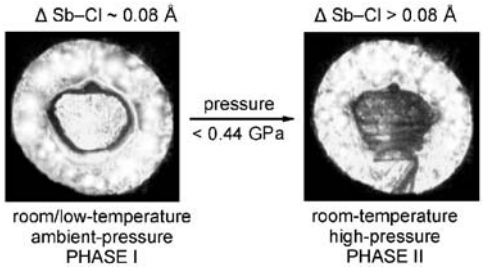

On cooling to 15 K $[(CH_3)_2NH_2]_2[SbCl_5]$ shows significant changes in the geometries of the longest Sb–Cl bonds that are correlated with the changes in the geometry of the N–H…Cl hydrogen bonds. Applying of quite modest pressures far exceed observed temperature-induced changes—$[(CH_3)_2NH_2]_2[SbCl_5]$ undergoes a first-order phase transition below ca. 0.44(5) GPa that destroys single-crystal samples.

---

^{151}Eu and ^{121}Sb Mössbauer spectroscopy of $EuSbSe_3$ and $EuBiSe_3$
Falko M. Schappacher, Rainer Pöttgen, Geng Bang Jin and Thomas E. Albrecht-Schmitt
page 3035

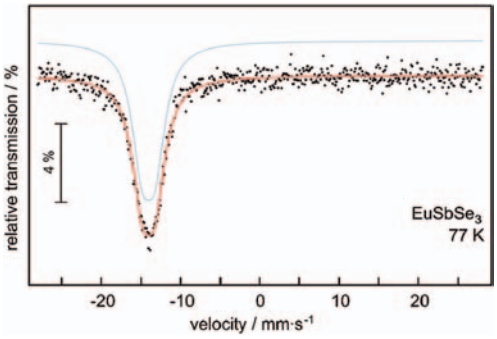

Experimental and simulated ^{121}Sb Mössbauer spectrum of $EuSbSe_3$ at 77 K.

Novel perovskite-related barium tungstate $Ba_{11}W_4O_{23}$
Seung-Tae Hong
page 3039

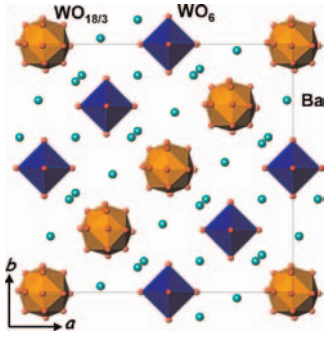

A slab of (0 0 1) plane around $z = 0$ with a thickness of ~5.0 Å for $Ba_{11}W_4O_{23}$. The oxide ions and the anionic vacancies on the $WO_{18/3}$ polyhedron are statistically distributed over three divided sites. Cation-vacancies are ordered in between adjoining $WO_{18/3}$ polyhedra.

Structural investigations of sol–gel-derived $LiYF_4$ and $LiGdF_4$ powders
S. Lepoutre, D. Boyer, A. Potdevin, M. Dubois, V. Briois and R. Mahiou
page 3049

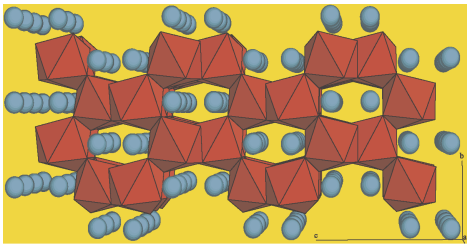

The sol–gel route is a soft process, which allows developing versatile-shaped compounds. A fluorine organic compound named 1,1,1-trifluoro-5-methyl-2,4-hexadione was used to synthesis $LiGdF_4$ and $LiYF_4$ powders based on the sol–gel method. These materials can be used as host lattices for rare-earth ions to provide phosphors.

Enhanced photoluminescence of Ba_2GdNbO_6: Eu^{3+}/Dy^{3+} phosphors by Li^+ doping
C.C. Yu, X.M. Liu, M. Yu, C.K. Lin, C.X. Li, H. Wang and J. Lin
page 3058

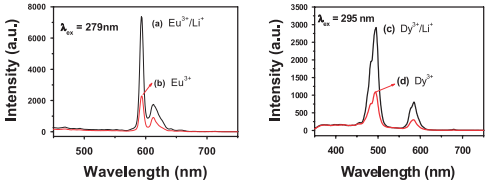

The Ba_2GdNbO_6: Eu^{3+}/Dy^{3+} and Li^+-doped Ba_2GdNbO_6: Eu^{3+}/Dy^{3+} phosphors were prepared by solid-state reaction. The incorporation of Li^+ ions into the Ba_2GdNbO_6: Eu^{3+}/Dy^{3+} phosphors has enhanced the photoluminescence intensities of Eu^{3+} and Dy^{3+}, depending on the doping concentration of Li^+.

Crystallochemistry of the novel two-layer *RE*$CuMg_4$ (*RE* = La, Tb) ternary compounds
P. Solokha, S. De Negri, V. Pavlyuk, A. Saccone and B. Marciniak
page 3066

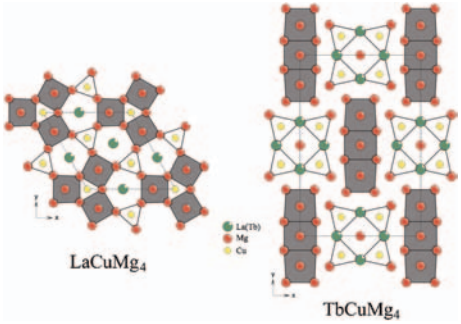

Slightly distorted body centered Mg blocks as structural motifs in the $LaCuMg_4$ and $TbCuMg_4$ compounds.

Continued

Synthesis and luminescent properties of Tb^{3+}-activated yttrium indium germanate phosphor
Yee-Shin Chang, Hui-Jan Lin, Yu-Chun Li, Yin-Lai Chai and Yeou-Yih Tsai
page 3076

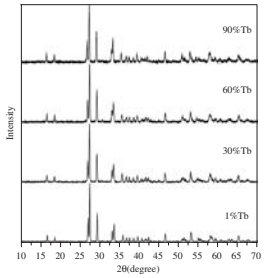

XRD profiles of $YInGe_2O_7$ doped with various contents of Tb^{3+} heated at 1300 °C for 10 h in air.

Composition- and temperature-dependent phase transitions in 1:3 ordered perovskites $Ba_{4-x}Sr_xNaSb_3O_{12}$
Qingdi Zhou, Brendan J. Kennedy, Margaret M. Elcombe and Ray L. Withers
page 3082

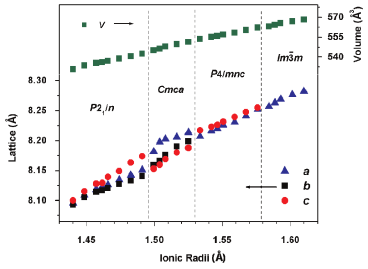

Diffraction studies of the series of $A_4NaSb_3O_{12}$ perovskites revel a complex series of temperature- and composition-dependent phase transitions, associated with both ordering of the Na and Sb cations and tilting of the octahedra.

Microstructure and electrical transport in nano-grain sized $Ce_{0.9}Gd_{0.1}O_{2-\delta}$ ceramics
Enrique Ruiz-Trejo, Jaime Santoyo-Salazar, Ruben Vilchis-Morales, Adriana Benítez-Rico, Francisco Gómez-García, Carlos Flores-Morales, José Chávez-Carvayar and Gustavo Tavizón
page 3093

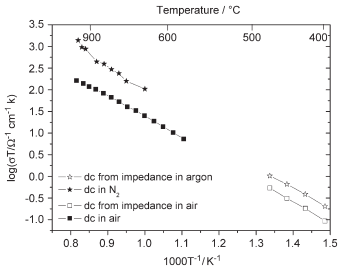

An enhancement of the electrical conductivity has been found in nano-grain sized $Ce_{0.9}Gd_{0.1}O_{2-\delta}$ ceramics in comparison with the most commonly accepted values of bulk ionic conductivity. We present the microstructural characterisation of the nanoparticles and the nanoceramics of $Ce_{0.9}Gd_{0.1}O_{2-\delta}$ and then we briefly discuss the possibilities of electron vs. oxygen ion conduction and grain boundary vs. bulk conductivity.

Sonochemical synthesis and luminescence properties of single-crystalline BaF_2:Eu^{3+} nanospheres
Ling Zhu, Jian Meng and Xueqiang Cao
page 3101

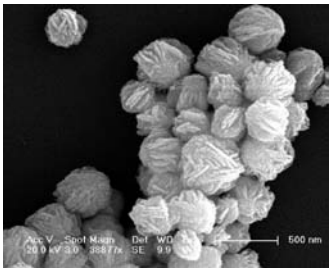

Single-crystalline BaF_2:Eu^{3+} (5.0 mol% Eu^{3+}) caddice spheres has been successfully synthesized via a facile, quick and efficient ultrasonic solution route employing the reactions between $Ba(NO_3)_2$, $Eu(NO_3)_3$ and KBF_4 under ambient conditions. This simple and unique synthetic method without any template or surfactant, which avoids the subsequent complicated workup procedures for the removal of the template or surfactant, has a potential advantage for synthesis of material with novel morphology.

A simple method to prepare ZnO and $Al(OH)_3$ nanorods by the reaction of the metals with liquid water
L.S. Panchakarla, M.A. Shah, A. Govindaraj and C.N.R. Rao
page 3106

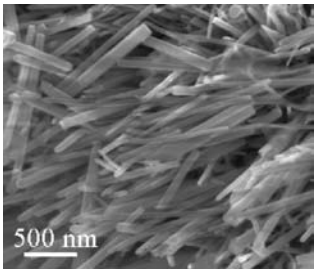

The reaction of water at a temperature in the 25–27 °C range with zinc metal gives rise to ZnO nanorods; with Al metal water gives $Al(OH)_3$ nanorods.

Synthesis and characterization of four new metal 5-phosphonoisophthalates discovered by high-throughput experimentation
Sebastian Bauer and Norbert Stock
page 3111

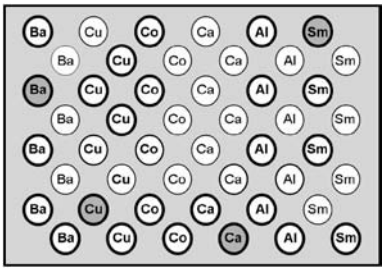

Applying high-throughput methods, the new ligand 5-diethylphosphonoisophtalic acid, $(HOOC)_2C_6H_3$-$PO_3(C_2H_5)_2$ (H_2Et_2L), was reacted with several di- and trivalent metal salts under hydrothermal conditions. Single-crystals of four new inorganic–organic hybrid compounds were isolated from the discovery library. The single-crystal structure analysis shows a varying M–O–M connectivity.

Hydrothermal synthesis, structural, Raman, and luminescence studies of Am[M(CN)$_2$]$_3 \cdot 3H_2O$ and Nd[M(CN)$_2$]$_3 \cdot 3H_2O$ (M = Ag, Au): Bimetallic coordination polymers containing both trans-plutonium and transition metal elements
Zerihun Assefa, Katrina Kalachnikova, Richard G. Haire and Richard E. Sykora
page 3121

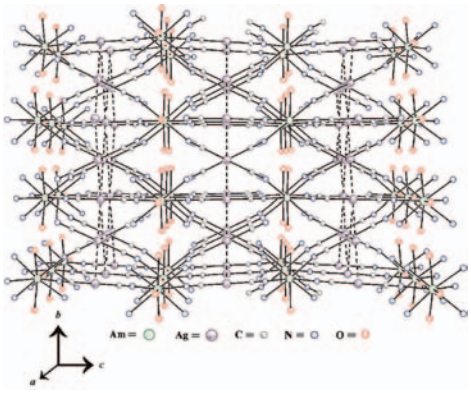

Coordination polymeric compounds between the "man-made" trans-plutonium element, americium, and transition metal ions were prepared using the hydrothermal synthetic procedure. The Am^{3+} ion and the transition metals, Au and/or Ag, are interconnected through cyanide bridging. The coordination around americium consists of six CN^- groups coordinated through the N atoms resulting in a trigonal prismatic environment. Three oxygen atoms of coordinated water molecules complete the tricapped trigonal prismatic coordination environment for Am^{3+}, providing a total coordination number of 9.

Local atomic structure of a zirconia-based americium transmutation fuel
Marcus Walter, Catharina Nästren, Joseph Somers, Regis Jardin, Melissa A. Denecke and Boris Brendebach
page 3130

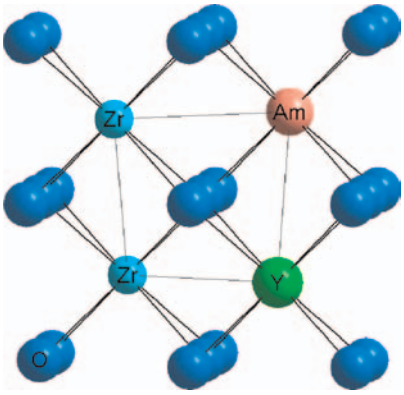

Local atomic structure in (Zr,Y,Am(III))O_{2-x}. The oxygen vacancies induced by Y and Am(III) dopant ions are associated with Zr atoms. Oxidation in air at 1000 °C contracts the Am(IV)–O bond, whereas the Zr environment relaxes.

Different aliphatic dicarboxylates affected assemble of new coordination polymers constructed from flexible–rigid mixed ligands
Xinxin Xu, Ying Ma and Enbo Wang
page 3136

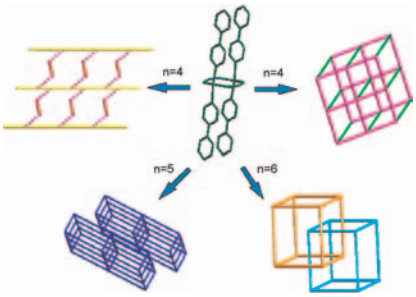

Seven complexes composed by 3D metal ions, aliphatic acid ligand and rigid bidentate nitrogen ligands: 4,4′-bpy, 2,2′-bpy and 1,10′-phen. With the change of the carbon number of the backbone of aliphatic dicarboxylate ligand, we can synthesize different complexes with various structures.

Selective-precursor reducing route to cobalt nanocrystals and ferromagnetic property
Changlong Jiang, Liyang Wang and Kunihito Kuwabara
page 3146

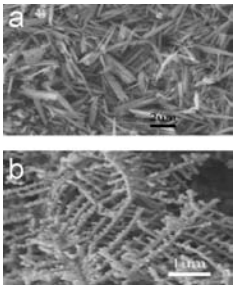

Nanorod bundles and three dimensional dendritic nanocrystal networks of Co nanocrystals were prepared at mild condition by selecting different precursors. Room temperature magnetic measure demonstrates much enhanced ferromagnetic property.

Titanium-based mixed oxides from a series of titanium(IV) citrate complexes
Yuan-Fu Deng, Hua-Lin Zhang, Qi-Ming Hong, Wei-Zheng Weng, Hui-Lin Wan and Zhao-Hui Zhou
page 3152

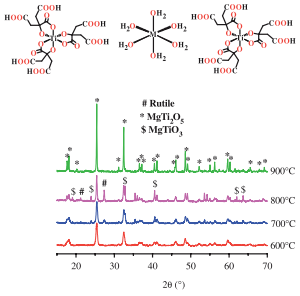

A series of heterobimetallic titanium citrate complexes with novel dodecameric water clusters were isolated and used as molecular precursors in an attempt to the preparations of mixed oxides MTi_2O_5.

Continued

A novel route to synthesize cubic $ZrW_{2-x}Mo_xO_8$ ($x = 0$–1.3) solid solutions and their negative thermal expansion properties

Ruiqi Zhao, Xiaojing Yang, Huiliang Wang, Jingsa Han, Hui Ma and Xinhua Zhao

page 3160

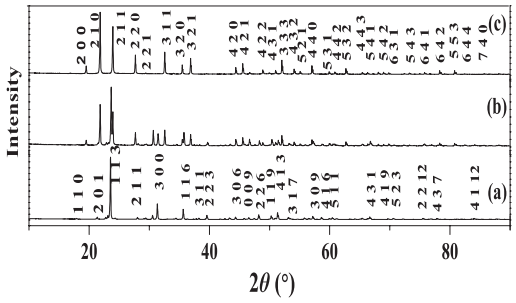

The trigonal precursor (a) is formed by calcining the dried coprecipitate of component oxides at 600 °C for 3 h. Through the trigonal precursor, cubic $ZrWMoO_8$ (c) is synthesized at 913–950 °C for 1 h. According to the novel preparation route, a series of cubic $ZrW_{2-x}Mo_xO_8$ ($x = 0$–1.3) are synthesized.

Crystal structure of $Ca_2Ln_3Sb_3O_{14}$ (Ln = La, Pr, Nd and Y): A novel variant of weberite

Y.S. Au, W.T. Fu and D.J.W. IJdo

page 3166

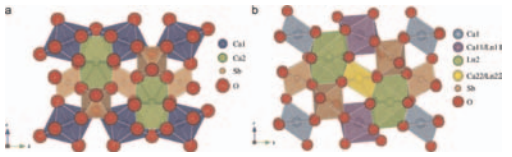

Schematic representations of the crystal structures of $Ca_2Sb_2O_6$ (left) and $Ca_2La_3Sb_3O_{14}$ (right) showing the arrangement of metal–oxygen polyhedrons.

Condensed rare-earth metal-rich tellurides. Extension of layered Sc_6PdTe_2-type compounds to yttrium and lutetium analogues and to Y_7Te_2, the limiting binary member

Laura M. Castro-Castro, Ling Chen and John D. Corbett

page 3172

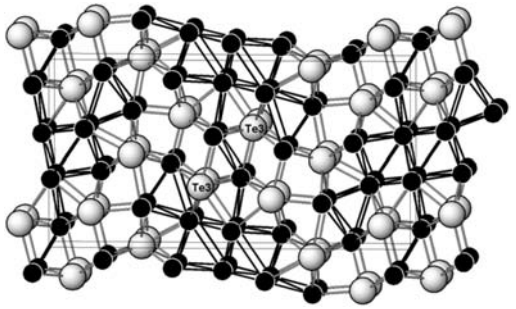

Substitutions at the same site in a common orthorhombic host structure convert the hypothetical Y_2Te (above) to eitherY_6ZTe_2 or the new binary Y_7Te_2.

Crystal structure and magnetic properties of complex oxides $Mg_{4-x}Ni_xNb_2O_9$, $0 \leqslant x \leqslant 4$

N.V. Tarakina, E.A. Nikulina, J. Hadermann, D.G. Kellerman, A.P. Tyutyunnik, I.F. Berger, V.G. Zubkov and G. Van Tendeloo

page 3180

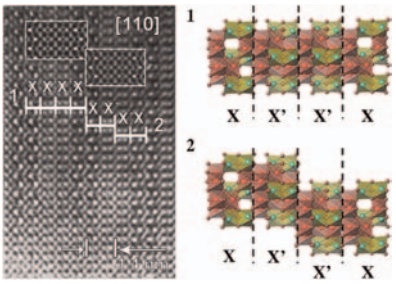

HREM image showing planar defects in $MgNi_3Nb_2O_9$ and their schematic representation.

Hydrothermal synthesis, characterization and its photoactivity of CdS/Rectorite nanocomposites

Jiangrong Xiao, Tianyou Peng, Ke Dai, Ling Zan and Zhenghe Peng

page 3188

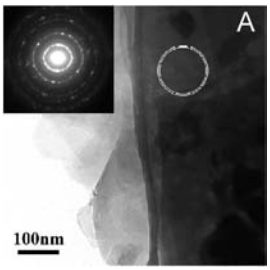

CdS/Rectorite nanocomposites were synthesized by hydrothermal method. Its absorptive property and photoactivity for Rhodamine B were enhanced significantly compared with that of the Rectorite. The nanocomposites are expected to be useful in various applications, for instance, adsorption and photodegradation of various organic contaminants.

Crystal structure, optical properties and colouring performance of karrooite $MgTi_2O_5$ ceramic pigments

Francesco Matteucci, Giuseppe Cruciani, Michele Dondi, Giorgio Gasparotto and David Maria Tobaldi

page 3196

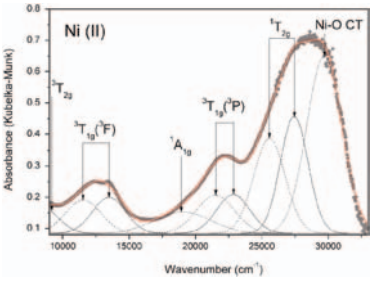

Karrooite is a promising ceramic pigment for high refractoriness and refractive indices. Incorporation of V(IV), Cr(IV), Mn(II) + Mn(III), Fe(III), Co(II) or Ni(II) in two crystallographically distinct octahedral sites affects unit cell parameters, bond length distances and cation order–disorder, leading also to distinct optical bands from the two different sites, so reducing colour purity.

Magnetic and thermoelectric properties of layered $Li_xNa_yCoO_2$
J.W.G. Bos, J.T. Hertz, E. Morosan and R.J. Cava
page 3211

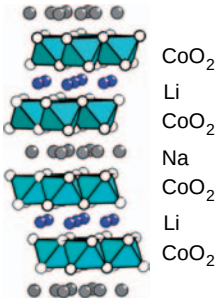

The ordered layered arrangement of Li^+ and Na^+ ions between CoO_2 sheets.

A highly coercive carbon nanotube coated with $Ni_{0.5}Zn_{0.5}Fe_2O_4$ nanocrystals synthesized by chemical precipitation–hydrothermal process
Huiqun Cao, Meifang Zhu, Yaogang Li, Jianhong Liu, Zhuo Ni and Zongyi Qin
page 3218

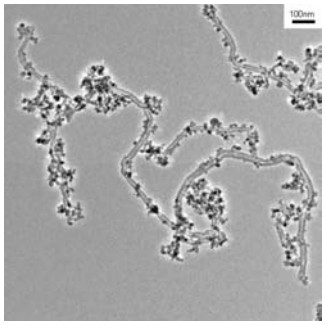

Novel magnetic composites ($Ni_{0.5}Zn_{0.5}Fe_2O_4$–MWCNTs) of multi-walled carbon nanotubes (MWCNTs) coated with $Ni_{0.5}Zn_{0.5}Fe_2O_4$ nanocrystals were synthesized by chemical precipitation–hydrothermal process. The composites had a high coercive field of 386.0 Oe, higher than those of MWCNT and $Ni_{0.5}Zn_{0.5}Fe_2O_4$ nanocrystals.

Syntheses and characterizations of complex perovskite oxynitrides $LaMg_{1/3}Ta_{2/3}O_2N$, $LaMg_{1/2}Ta_{1/2}O_{5/2}N_{1/2}$, and $BaSc_{0.05}Ta_{0.95}O_{2.1}N_{0.9}$
Young-Il Kim and Patrick M. Woodward
page 3224

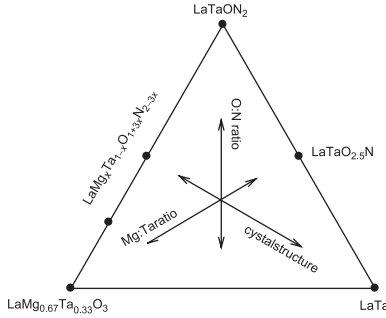

Phase diagram showing the relations among composition and crystal structure in the quaternary La–Mg–Ta–O–N system.

Atomic and vacancy ordering in carbide ζ-Ta_4C_{3-x} ($0.28 \leqslant x \leqslant 0.40$) and phase equilibria in the Ta–C system
A.I. Gusev, A.S. Kurlov and V.N. Lipatnikov
page 3234

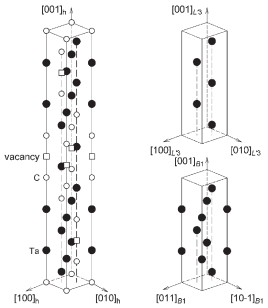

Ordered distribution of carbon atoms C and structural vacancies in a unit cell of the trigonal (space group $R\bar{3}m$) ζ-Ta_4C_{3-x} phase. The closely packed metal sublattice in carbide ζ-Ta_4C_{3-x} consists of alternating blocks where Ta atoms are located in the same manner as on the FCC sublattice of the cubic carbide TaC_y and the HCP sublattice of the hexagonal carbide Ta_2C_y.

Water-containing derivative phases of the $Sr_{n+1}Fe_nO_{3n+1}$ series
M. Lehtimäki, A. Hirasa, M. Matvejeff, H. Yamauchi and M. Karppinen
page 3247

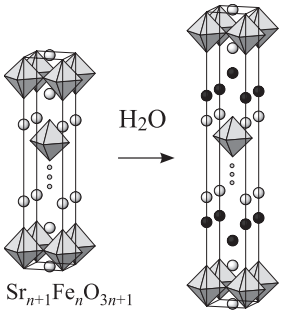

Water-containing derivative phases obtained from the homologous series of $Sr_{n+1}Fe_nO_{3n+1}$ Ruddlesden–Popper phases through topotactic water intercalation.

Electronic state of ^{57}Fe used as Mössbauer probe in the perovskites $LaMO_3$ (M = Ni and Cu)
Igor Presniakov, Gérard Demazeau, Alexei Baranov, Alexei Sobolev, Tatyana Gubaidulina and Viyacheslav Rusakov
page 3253

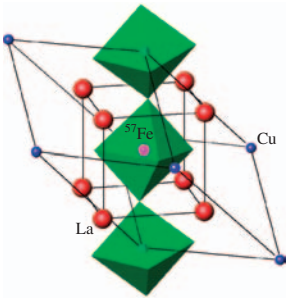

Mössbauer spectroscopy study of $LaCuO_3$ doped with the Mössbauer probe ^{57}Fe.

Continued

Rapid solid-state synthesis of binary group 15 chalcogenides using microwave irradiation
Christine Mastrovito, Jonathan W. Lekse and Jennifer A. Aitken
page 3262

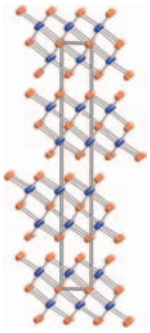

Solid-state microwave synthesis offers a fast, economical and green route for the preparation of Sb_2Se_3, Sb_2Te_3, Bi_2Se_3 and Bi_2Te_3 (shown in graphic) in only 4 min. Through the process of preparing these materials in pure form, the effects that several reaction variables, including sample quantity, irradiation time and sample geometry, have on the outcome of the reactions were documented.

On the structure and microstructure of "$PbCrO_3$"
Ángel M. Arévalo-López and Miguel Á. Alario-Franco
page 3271

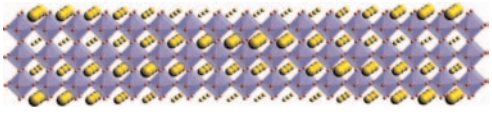

Model of the structure of $PbCrO_3$ obtained by electron microscopy and diffraction.

***Ab initio* study on structure and phase transition of *A*- and *B*-type rare-earth sesquioxides Ln_2O_3 (*Ln* = La–Lu, Y, and Sc) based on density function theory**
Bo Wu, Matvei Zinkevich, Fritz Aldinger, Dingzhong Wen and Lu Chen
page 3280

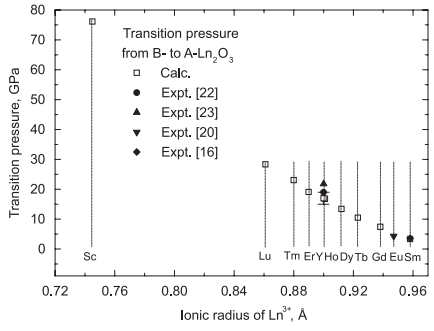

This graph shows the calculated transition pressure with respect to the transition of the Ln_2O_3 from its *B*- to *A*-type together with the available experimental data superimposed. The transition pressure was obtained by calculating the common tangent slope of the two fitted *E*–*V* curves based on the empirical third-order Birch–Murnaghan equation of state.

Aqueous mineralization process to synthesize uniform shuttle-like $BaMoO_4$ microcrystals at room temperature
Xueying Wu, Jin Du, Haibo Li, Maofeng Zhang, Baojuan Xi, Hai Fan, Yongchun Zhu and Yitai Qian
page 3288

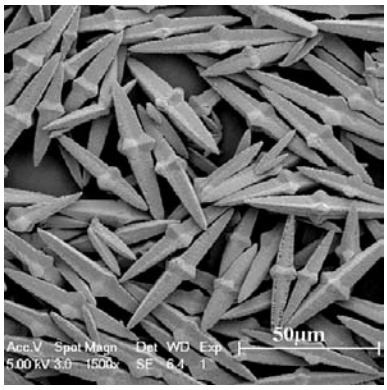

A facile aqueous mineralization process has been used to synthesize uniform shuttle-like $BaMoO_4$ microcrystals at room temperature. High quality, large scale, and uniform microcrystals with a mean length size of 50 μm can be easily obtained. These microcrystals exhibit single-crystal nature and perfect symmetry.

"Unusual Ln^{3+} substitutional defects": The local chemical environment of Pr^{3+} and Nd^{3+} in nanocrystalline TiO_2 by Ln–K edge EXAFS
Paolo Ghigna, Adolfo Speghini and Marco Bettinelli
page 3296

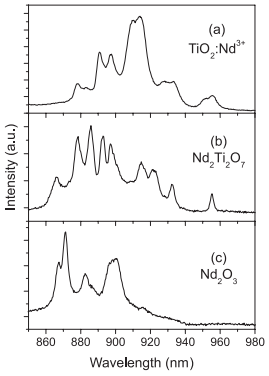

Comparison between the room temperature emission spectra of the Nd^{3+} doped TiO_2 nanocrystalline sample (a), the $Nd_2Ti_2O_7$ sample (b) and a commercial Nd_2O_3 sample (c) ($\lambda_{exc} = 355$ nm).

Continued

Icosahedral Li clusters in the structures of $Li_{33.3}Ba_{13.1}Ca_3$ and $Li_{18.9}Na_{8.3}Ba_{15.3}$
Volodymyr Smetana, Volodymyr Babizhetskyy, Constantin Hoch and Arndt Simon
page 3302

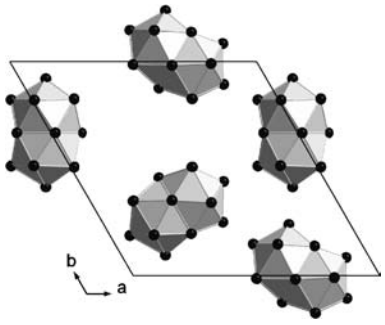

The intermetallic phases $Li_{33.3}Ba_{13.1}Ca_3$ and $Li_{18.9}Na_{8.3}Ba_{15.3}$ have been prepared and their crystal structures have been determined. According to single-crystal X-ray diffraction data, both compounds crystallize in new structure types with trigonal unit cells ($Li_{33.3}Ba_{13.1}Ca_3$: $R\bar{3}c$, $a=19.9127(4)$ Å, $c=90.213(3)$ Å, $Z=18$, $V=30{,}978(1)$ Å^3 and $Li_{18.9}Na_{8.3}Ba_{15.3}$: $P\bar{3}$, $a=20.420(3)$ Å, c=92.914(19), $Z=18$, $V=33{,}550(10)$ Å^3). Both compounds contain icosahedron-based polytetrahedral clusters, typical for Li-rich phases, e.g. $Ba_{19}Li_{44}$.

Rietveld refinement and photoluminescent properties of a new blue-emitting material: Eu^{2+} activated $SrZnP_2O_7$
Jun-Lin Yuan, Xiao-Yan Zeng, Jing-Tai Zhao, Zhi-Jun Zhang, Hao-Hong Chen and Guo-Bin Zhang
page 3310

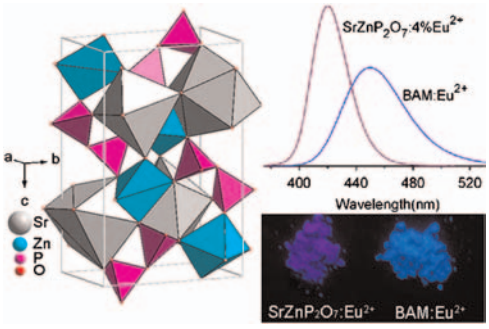

The perspective view of $SrZnP_2O_7$ unit cell, which was obtained from Rietveld refinement. Eu^{2+} activated $SrZnP_2O_7$ is a new violet–blue emitting phosphor that has efficiency as high as 96% as that of BAM:Eu^{2+}.